Measurements of noninterceptive fluorescence profile monitor prototypes using 9 MeV deuterons

J. M. Carmona,* I. Podadera, and A. Ibarra
Centro de Investigaciones Energéticas, Medioambientales y Tecnológicas (CIEMAT), E-28040, Madrid, Spain

A. Bocci, M. C. Jiménez-Ramos, J. García López, and Z. Abou-Haïdar
Centro Nacional de Aceleradores (CNA), E-41092, Seville, Spain

M. A. G. Álvarez and B. Fernández
Departamento de Física Atómica, Molecular y Nuclear (FAMN), Universidad de Sevilla, E-41012, Seville, Spain
(Received 1 February 2011; published 17 July 2012)

Two types of noninterceptive optical monitors, based on gas fluorescence, have been designed for use on the Linear IFMIF Prototype Accelerator (LIPAc) that is currently under development (a 125 mA, 9 MeV, 175 MHz continuous wave deuteron beam). These diagnostics offer a technique to characterize the transverse beam profile for medium to high current hadron beams, without intercepting the beam core. This paper reports on beam tests using the prototype monitors developed for LIPAc. Tests were carried out at an experimental line of the Centro Nacional de Aceleradores cyclotron, using 9 MeV deuterons with beam currents from 0.4 to 40 μA. In addition, transverse beam profile measurements were performed under high background radiation (e.g. gamma dose rate up to 83 mSv/h). Preliminary cross-checks with different profilers, as well as a systematic scan of beam current and vacuum pressures and tests with different injected gases (nitrogen and xenon) have been performed. In this work, we present a brief description of the experimental setup and the first measurements obtained with these prototype profilers plus a discussion of the first analysis of the background signal in a detector as a function of radiation background.

DOI: 10.1103/PhysRevSTAB.15.072801 PACS numbers: 29.20.Ej, 29.20.dg, 29.27.Fh

I. INTRODUCTION

A high power beam, such as the 1.125 MW Linear IFMIF prototype Accelerator (LIPAc) beam [1], is potentially harmful for any interceptive diagnostic (even when operated at a low duty cycle), especially if it intercepts the beam core. In such cases, noninterceptive diagnostics are preferrable. It is foreseen that in the LIPAc, two noninterceptive beam profilers will be installed, one based on residual gas fluorescence and the other on residual gas ionization. This present article focuses on the fluorescence beam profiler.

In general, beam particles passing through a vacuum pipe may excite residual or injected gas particles in the vacuum chamber and the beam path, thereby producing photons as a consequence of deexcitation. The resultant light can be used to determine the beam profile without the need to intercept the beam. This technique has previously been tested on other machines, e.g., the high energy proton synchrotron CERN-PS [2,3], the relativistic heavy ion collider RHIC [4], and the heavy ion GSI-UNILAC [5].

At present, several projects involving the construction and exploitation of high current and medium energy deuteron accelerators are in progress (i.e., SARAF, IFMIF, SPIRAL2). These accelerators provide a high peak power deposition, making the use of interceptive monitors unfeasible during nominal power operation. To our best knowledge, noninterceptive profile measurements of deuteron beams are not reported in literature, at least not in the MeV energy range. Hence, the results presented here may be the first deuteron beam profile measurements performed using a noninterceptive optical method.

In this work, two prototype fluorescence profile monitors (FPMs), designed and developed at CIEMAT [6], were tested at the Centro Nacional de Aceleradores (CNA), Spain [7], where the beam profiling tests were performed with a 9 MeV deuteron beam.

Experiments were performed to mimic the beam parameters of the LIPAc as closely as possible [1]. Although the beam current was rather low (≤ 40 μA), other critical parameters, such as energy, cross sections, transition branching ratios, efficiencies, etc., are the same, with the exception of vacuum pressure. As the number of photons produced during beam-gas interaction is expected

*jm.carmona@ciemat.es

to increase linearly with beam current and vacuum pressure [8], an extrapolation of the number of counts to high current scenarios is assumed to be straightforward.

II. FPM PROTOTYPES

The prototype FPMs are based on a custom intensified charge injection device (ICID) camera and a linear photomultiplier tube (PMT) array. In the text, we refer to the former prototype by ICID-FPM and to the latter by PMT-FPM. A brief description of both monitors is provided in the following subsections.

A. Custom ICID-FPM

The custom intensified camera employs a radiation resistant charge injection device (CID) camera instead of a standard CCD. CID cameras minimize single event transfer inefficiencies in intense radiation environments and guarantee sensor readings at high doses (i.e., 3 Mrad). The CID camera selected is a model 8726DX6 by Thermo Scientific [9]. The CID camera was coupled to an image intensifier by Proxitronic [10]. Specifications of the CID and image intensifier are listed in Tables I and II. The Proxitronic intensifier unit has a double stack multichannel plate (MCP) sandwiched between a photocathode and a phosphor screen. We refer to the complete system as the intensified charge injection device (ICID).

The gain of the intensifier can be controlled by the MCP voltage from 10^2 to 10^6. This voltage is generated by a Proxitronic control unit which also provides a gating pulse. The integration time can follow the period of an external transistor-transistor logic signal or can be preset to a fixed time. Short integration times and fast synchronization can therefore be achieved, see Table II.

TABLE I. Specifications of the 8726DX6 CID camera.

Displayed pixels	726×575
Pixel size	$17.3\ \mu m \times 17.3\ \mu m$
SN ratio	-45 dB signal/rms
Geometric distortion	0%
Radiation tolerance	3 Mrad (at least)
Cable length (control head)	up to 50 m
Video output	Analog and digital

TABLE II. Specifications of the Proxitronic MCP intensifier.

Transmission window	Quartz
Input diameter	25 mm
Photocathode	Bialkali (K_2SbCs)
MCP type	V-stack
Phosphor	P46
MCP maximum voltage (recommended)	1800 V
MCP maximum gain	10^6
Shortest gate time	100 ns
Maximum trigger frequency	14 kHz

B. Custom PMT-FPM

The second prototype is based on a linear multianode PMT array coupled to a lens. A 32 channel PMT model H7260, by Hamamatsu Photonics [11], was selected. The main specifications are listed in Table III. A pure quartz input window was selected rather than the standard borosilicated window in order to minimize transmission losses due to irradiation. The electronic data acquisition system (DAQ) for the PMT array is a PhotoniQ model IQSP482 from Vertilon Corp. (Table IV). The DAQ interface facilitates normalization of the PMT channel outputs to correct any channel to channel sensitivity variations.

The gain of the PMT channels can be regulated by changing the voltage supplied to the metal channel dynodes. In this case, varying the voltage from 500 to 900 V increases the amplification factor from 2×10^4 to 6×10^6. After current amplification by the PMT, the DAQ system performs charge integration and digitalization, and returns the total integrated charge level (in pico-Coulomb) for each channel. In conjunction with the PMT, the DAQ system permits the capture of narrow charge pulses with single photon sensitivity. The PMT voltage, operational modes, and integration times can be configured from the interface software of the PhotoniQ DAQ system.

The PMT array is mounted on a movable board placed in a light tight housing with a standard F mount adaptor for mounting an objective lens. The movable board allows correct focusing with different lenses.

TABLE III. Specifications of the H7260 multianode PMT array.

Transmission window	Quartz
Photocathode	Bialkali
Number of channels	32
Area per channel	0.8×7 mm
Channel pitch	1 mm
Channel cross-talk	3%

TABLE IV. Specifications of the PhotoniQ IQSP482 data acquisition system.

Number of channels	64
Resolution	16 bits
Dynamic range	96 dB
Input noise charge	30 fC rms typical
Channel cross-talk	-84 dB typical
Maximum trigger rate	120 kHz
Minimum event pair resolution	7 μs maximum

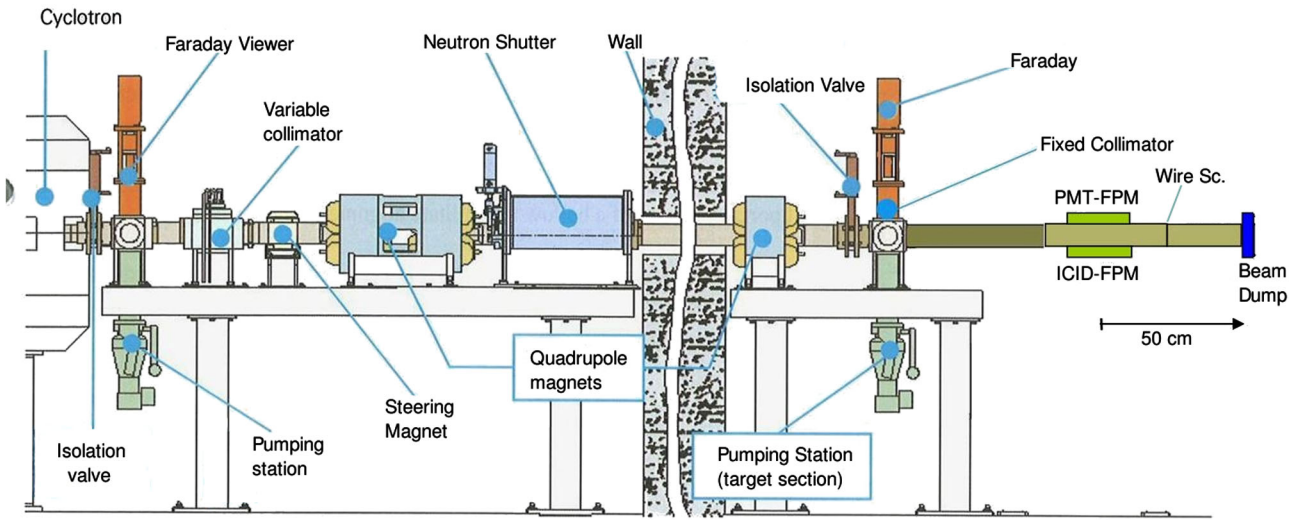

FIG. 1. Layout of the experimental line and diagnostics of the CNA cyclotron.

III. EXPERIMENTAL SETUP

The FPM prototypes were installed on the experimental line of the CNA cyclotron, just upstream from the rotating wire scanner (BPM-83 from NEC Corp., operating in secondary electron mode) in order to perform a first cross-check between profilers. See Fig. 1. The experimental line is located in a shielded room, separated from the cyclotron. Inside and outside this room, gamma and neutron detectors are installed for personnel safety. A triplet magnet is installed for final beam shaping. A fixed (15 mm diameter) collimator is located downstream from the triplet. In addition, between the collimator and the beam profilers, two movable scintillators allow the beam shape to be checked.

In addition, a beam dump, consisting of aluminum plus 1 mm of graphite, is located at the end of the line. Finally, both FPMs were installed in a horizontal position to view the vertical projection of the beam at the same point, one from left and the other from right.

After installing the diagnostics, the ICID-FPM was calibrated by inserting a calibration pattern (a simple ruler) in the center of the beam pipe, with low level, nonuniform ambient lighting. The PMT-FPM was calibrated against the ICID-FPM prototype due to the lack of a dedicated *in situ* calibration system. A specific calibration pattern is being developed for the PMT device and will be reported in future work.

TABLE V. Optical parameters for ICID-FPM and PMT-FPM.

Parameter	Units	ICID	PMT
Focal length	[mm]	25	50
f/number		2.8	2.8
FOV	[mm]	181	250
β_y		0.55	0.79
Calibration	[mm/(pixel, channel)]	0.315	7.8
Depth of field	[mm]	± 30	...

With respect to the optics, a 25 mm focal length lens (model Megapixel by Edmund Optics, England) was chosen for the ICID-FPM whereas a Carl Zeiss Planar T* 1.4/50 mm lens was selected for the PMT-FPM. The various parameters related to the calibration of the FPMs are listed in Table V, i.e., the focal lengths of the lenses, their f number, the maximum field of view (FOV), the total scale factor of the system for the y axis (β_y), the calibration factor for each prototype, and the depth of focus for ICID. The calibration factor agrees well with calibrations performed with a pencil lamp on an optical laboratory testbench thereby providing a cross-check. For beam profile measurements, the depth of focus should cover at least the beam diameter in order to minimize broadening effects. If needed, the depth of focus can be increased by stopping down the f number at the expense of signal. The present compromise between f number and signal strength seems to be adequate for the current range of beam sizes.

As we were interested in obtaining good statistics, we did not employ a filter for these measurements. Hence, the detectors collected photons across the whole visible spectrum. Thus, the contribution of each transition in the final profile will be a convolution of the spectral line emission intensity with the spectral efficiency of each detector. The maximum spectral response of both detectors lies between 370–460 nm [10,11]. The most intense nitrogen line transitions lie in the same spectral region (e.g., 391.4 and 427.3 nm) [2,5], hence the system is considered to be optimized.

IV. SIMULATING HIGH CURRENT SCENARIOS

The emissivity ξ, see Eq. (1), due to the interaction of beam ions with residual gas can be expressed as the number of photons emitted per second per path length (d_{path}). It

also depends on the beam current, I_{beam}, the number of residual gas particles within the beam-gas interaction volume (pressure P_{gas}), and the total cross section, σ, for photon transitions (excitation plus deexcitation of the gas particles). The number of detected photons [Eq. (2)] and, more specifically, the number of counts, N, collected by a detector depends on the emissivity, ξ, the solid angle, Ω, the integration time, T, and the system efficiency, η_{sist}:

$$\xi \propto \sigma P_{\text{gas}} I_{\text{beam}} d_{\text{path}} \tag{1}$$

$$N \propto \xi \Omega T \eta_{\text{sist}}. \tag{2}$$

In order to simulate LIPAc conditions, i.e., same cross sections and branching ratios, the tests are performed with 9 MeV deuterons. The main parameters at CNA match those of LIPAc, with the exception of the lower current; but in view of the above, the low currents can be compensated for by increasing the gas pressure. Indeed, the emissivity can be increased by changing the number of particles involved in the interaction, i.e., by increasing the beam current or the gas pressure [Eqs. (1) and (2)]. Thus, the results obtained in these experiments can be extrapolated to higher current deuteron beams in a straightforward manner.

In order to check that wide beam profiles are accessible to this technique, it was preferable to use a beam with large transverse size in these initial experiments. Usually, the beam is widened just upstream from the beam stop to reduce the deposition power density. At the same energy and beam current, wide profiles are more difficult to measure because of the smaller photon density (and a poorer signal to noise ratio).

V. MEASUREMENTS WITH DEUTERONS

Before proceeding to the analysis, in this section we present the first runs and comment on each profile prototype, including a profile cross-check with a traditional interceptive profiler (i.e. a wire scanner).

A. PMT-FPM first runs

From the first tests, it was evident that the PMT-FPM prototype was capable of measuring profiles with lower beam currents than the ICID-FPM prototype. Figure 2(a) shows a beam profile recorded by the former using a 9 MeV, 400 nA deuteron beam. For this, the pressure in the diagnostic chamber was 3.6×10^{-4} mbar when using nitrogen (N_2). Under these conditions, a clear beam profile was obtained. The PMT voltage was set at its maximum value while the total integration time was 100 ms.

The beam width $\sigma(y)$, obtained from a Gaussian fit to the data, was 10.2 ± 0.4 mm. This error is the fit error, giving the 1-σ confidence bound for the beam width. To demonstrate the standard deviation of the beam width measurements under these conditions, 20 samples with 100 ms of integration time are plotted in Fig. 2(b).

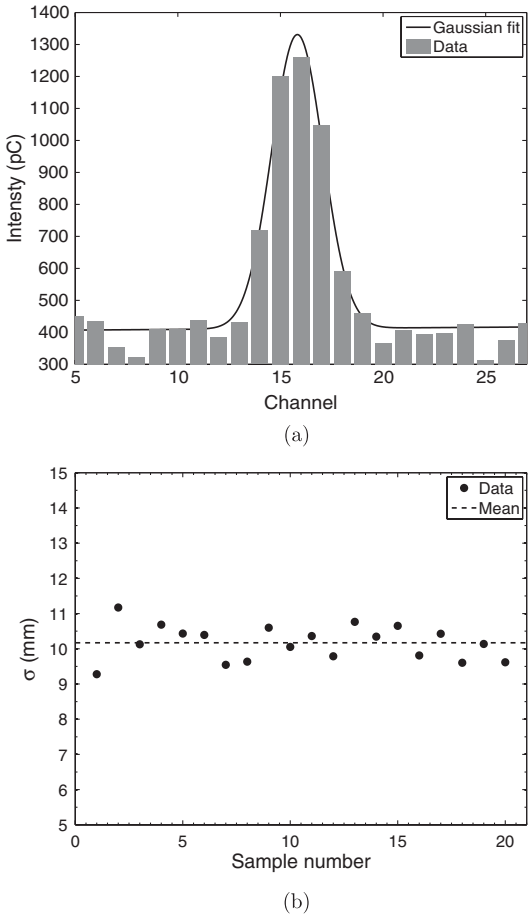

FIG. 2. First profile acquired (a) with the PMT-FPM prototype for a D^+ current of 400 nA and a N_2 pressure of 3.6×10^{-4} mbar. 20 consecutive beam profile samples are analyzed (b) to check the standard deviation of the beam widths [σ(mm)] in such conditions.

Again, the beam width $\sigma(y)$ is determined by a Gaussian fit for each sample. The mean of the beam widths is 10.17 mm whereas the standard deviation of the beam widths [SD(σ)], is 0.49 mm, resulting in 10.2 ± 0.5 mm. Better photon statistics (higher signal levels) reduces the [SD(σ)] improving the precision of the measurements.

As noted, the pressure level during these experiments (around 10^{-4} mbar) was chosen to compensate for the low beam current (0.4–40 μA) and hence to simulate higher beam current scenarios (i.e., 125 mA for LIPAc). Because of the linear relation between beam current and photon statistics (see Sec. VI A), it is considered that the pressure levels typically found in LINACs (10^{-6}–10^{-8} mbar) will suffice for operation of FPM profilers.

B. ICID-FPM first runs

Figure 3 shows a picture of the vacuum chamber, recorded by the ICID-FPM without the beam, using external illumination from a nearby viewport. Two circles delimit both viewports, the ICID-FPM viewport (large circle) and

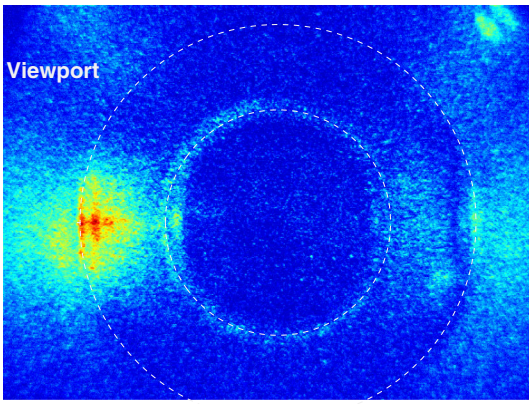

FIG. 3. Image of the vacuum chamber obtained by the ICID-FPM. The larger circle delimits the ICID-FPM viewport whereas the small circle delimits the PMT-FPM viewport. Wall reflections are seen clearly.

the PMT-FPM viewport (small circle). Reflections off the beam pipe walls are visible. Pixels outside the smaller circle can be affected by wall reflections during profiler operation. Hence, the area within the small circle is taken as the region of interest (ROI) where the contribution of light reflections on the beam profile is reduced. A blackened chamber will further minimize light reflections, permitting a larger ROI (i.e., the large circle).

Two beam images [Figs. 4(a) and 4(c)] and their corresponding transverse beam profiles [Figs. 4(b) and 4(d)] are shown for different experimental conditions (and detector setup). Here, the small circle has been taken as the ROI for the transverse profile. The beam is clearly visible in both cases, and a fit to each profile gives a beam width of $\sigma = 7.1$ mm.

The gain (MCP voltage) of the ICID-FPM prototype has to be adjusted for the different experiments to obtain the best possible image. As beam current increases, a lower amplification can be used, resulting in a profile with reduced noise. In contrast, a high MCP voltage can easily saturate the detector at high beam currents.

C. Beam profile cross-checking

Preliminary cross-checks between the FPM prototypes and a wire scanner were performed (see Fig. 5). The beam conditions for the series Figs. 5(a)–5(c) were a beam current of 15 μA, a nitrogen pressure of 7×10^{-4} mbar, and a wider beam. The voltage applied to the MCPs of the

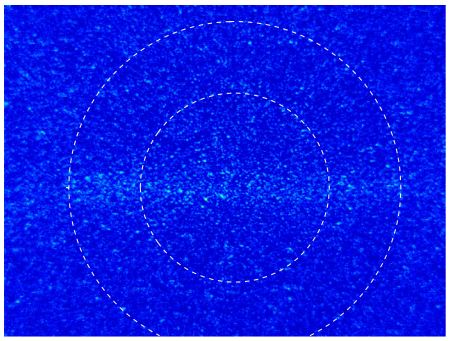

(a)

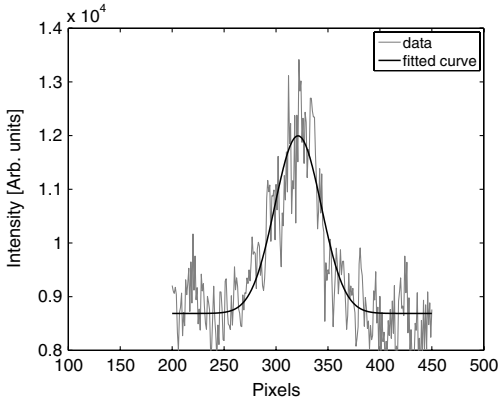

(b)

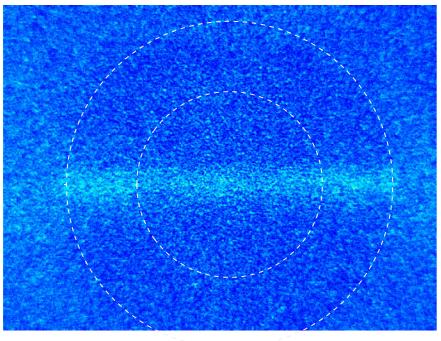

(c)

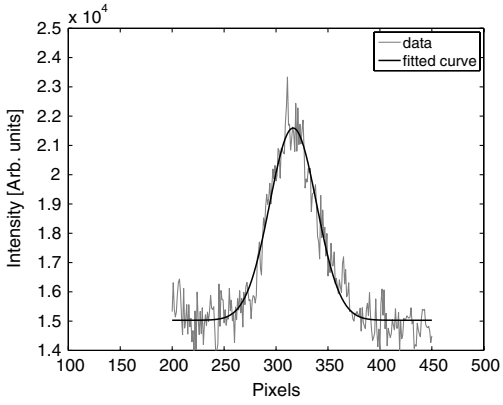

(d)

FIG. 4. Beam images (left) and corresponding profiles (right) without treatment. Experimental conditions are (a) beam intensity 2.5 μA, pressure 8.7×10^{-4} mbar, MCP voltage 1700 V, (c) beam intensity 20 μA, pressure 7.4×10^{-4} mbar, MCP voltage 1600 V. Beam widths are $\sigma = 7.1 \pm 0.6$ mm for (b) and $\sigma = 7.1 \pm 0.3$ mm for (d).

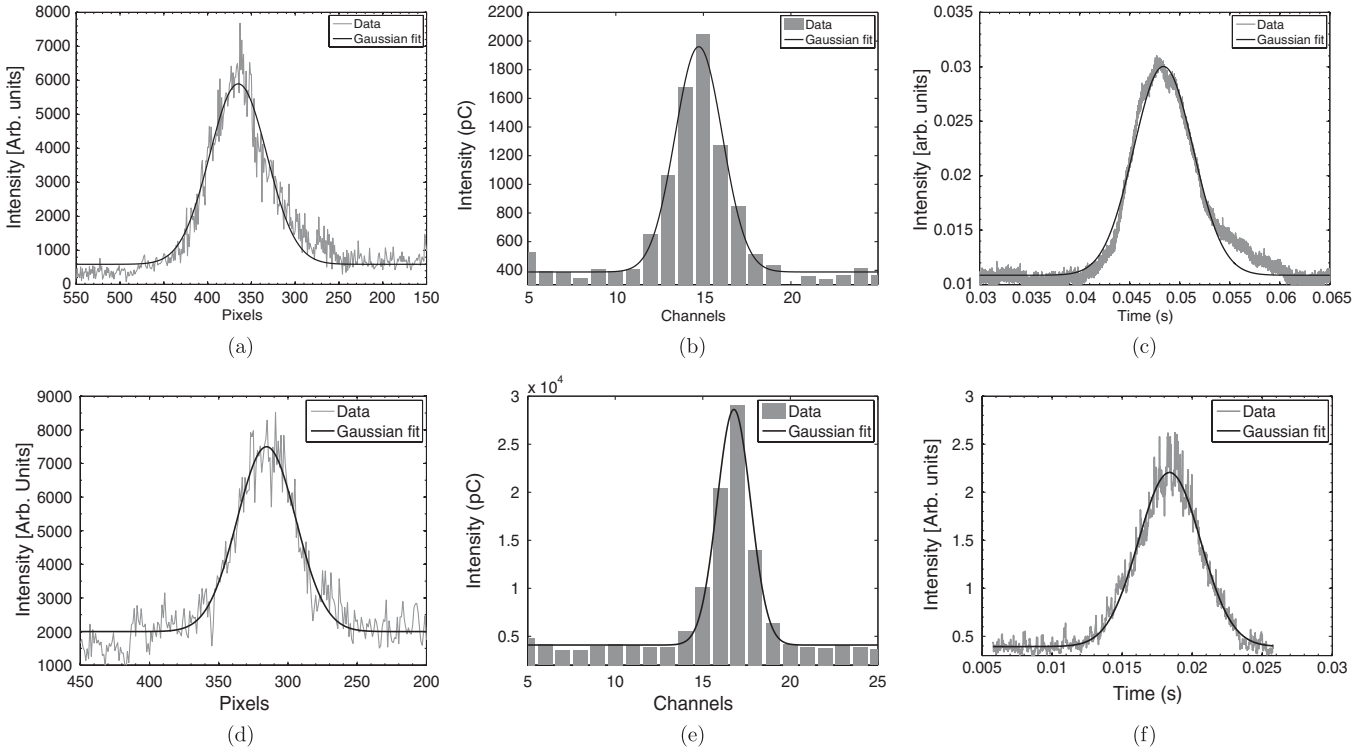

FIG. 5. Transverse beam profiles for a D^+ current of 15 μA (top) and 10 μA (bottom) recorded by the ICID-FPM prototype (a),(d), the PMT-FPM prototype (b),(e) and the wire scanner (c),(f). A Gaussian curve is fitted to the data. The transverse beam sizes [σ(rms)] obtained from the fits are $\sigma = 10.3 \pm 0.1$ mm (a), $\sigma = 10.5 \pm 0.5$ mm (b), and $\sigma = 10.40 \pm 0.01$ mm (c) for the top, and $\sigma = 6.8 \pm 0.2$ mm (d), $\sigma = 7.4 \pm 0.4$ mm (e), and $\sigma = 7.61 \pm 0.01$ mm (f) for the bottom.

ICID camera was 1580 V. Integration times for the ICID-FPM and PMT-FPM were 20 and 5 ms, respectively. The beam conditions for the bottom series [Figs. 5(d)–5(f)] were 10 μA, 8.7×10^{-4} mbar, and a smaller beam. The voltage applied to the MCPs of the ICID camera was 1700 V. Integration times for the ICID-FPM and PMT-FPM were 20 and 100 ms, respectively. Beam profiles obtained with the wire scanner [Figs. 5(c) and 5(f)] are also shown for comparison. The beam widths obtained with each type of profiler are shown in the caption. The higher noise found in Fig. 5(d), as compared to Fig. 5(a), is due to the higher amplification factor applied to the MCP to compensate the lower beam current.

The beam widths for the various profiles shown in Fig. 5 are in reasonable good agreement. Moreover, the recorded profile shapes are similar, with only a slight deviation from the Gaussian curve on the right in the top series example.

D. Extrapolations to LIPAc

Using the profile of Fig. 2, the pulse length required for measuring a similar profile in LIPAc (9 MeV, 125 mA) can be estimated. If the product between the beam current, the pressure, and the acquisition time (or beam pulse) is assumed equal (see Sec. IV), then it should be possible to obtain a profile with similar quality.

For the parameters of Fig. 2, we obtain 4×10^{-4} mA $\times$ 3.6×10^{-4} mbar $\times$ 100 ms $= 1.44 \times 10^{-5}$ [mA mbar ms]. Comparing this value to the LIPAc case, i.e. 125 mA $\times$ 10^{-6} mbar $\times$ t_{pulse}, it will be possible to measure a beam with a single pulse length (t_{pulse}) of 115 μs, (0.01% of duty cycle). For these calculations, a pressure of 10^{-6} mbar has been assumed, although any pressure could be used (e.g. for 10^{-7} mbar, the corresponding pulse length would be $\sim$1.2 ms). Similarly, for monitors located at the end of the LIPAc line (at a pressure of 10^{-5} mbar under nominal conditions), the corresponding pulse length would be 11.5 μs.

The same extrapolation can be applied to Figs. 5(a) and 5(b). Again, if the product of beam current, pressure, and integration time is assumed equal, a reference value for integration time needed to replicate similar profiles in LIPAc can be estimated. For the ICID-FPM prototype, a 1.7 ms beam pulse (or integration time) will be required, whereas a 420 μs pulse will be required for the PMT with the same detector settings. The reference pressure used in these estimations is 10^{-6} mbar.

This assumption of linearity for current and pressure is analyzed in the next section.

VI. CURRENT AND PRESSURE SCANS

Two scans were performed in order to check the linearity of the relation between the profile amplitude, the

beam current, and the gas pressure. These scans are also used to study the dependence of the profile beam width on beam current and vacuum pressure for 9 MeV deuterons. The reliability of the fluorescence technique is discussed below. The scans were systematic, i.e., changing only one parameter at a time during the sets of measurements.

The experimental data, see Figs. 6 and 7, were recorded using the PMT-FPM prototype as the amplification factor could be kept constant during both scans [independently of the background radiation (B_R) level] without pushing the detector into saturation. With the ICID-FPM, it was necessary to vary the amplification factor (MCP voltage) due to noise and/or image saturation.

A. Beam current scan

The nitrogen pressure inside the diagnostic chamber was held at 2.3×10^{-4} mbar during the current scan. This value guaranteed good profile measurements at the lowest current setting of the scan (i.e., 400 nA). For the scan the deuteron beam current was varied between 400 nA and 32 μA. In all cases, the total integration time for the PMT-FPM was 100 ms, while the voltage was set for maximum gain.

Beam profiles are shown in Fig. 6(a) as a function of beam current. The evolution of the integrated profile intensity (sum of the intensity measured by each PMT channel minus background signal per channel) and the beam width, $\sigma(y)$, versus the deuteron current are shown in Figs. 6(b) and 6(c), respectively, where the expected linear relation between the profile intensity and the beam current is confirmed [see Fig. 6(b)]. A linear fit was performed to the data to highlight the tendency and a slope of 2.74×10^3 pC/μA was found.

In addition, Fig. 6(c) shows that the beam width (as determined by a Gaussian fit) tends to remain constant when increasing the beam current from 0.4 to 32 μA. The mean value is 8.3 mm with a standard deviation of 0.9 mm (8.3 $\pm$ 0.9 mm). The variation of the beam width is larger at low beam currents as a consequence of lower signal strength. The standard deviation drops to 0.4 mm for beam currents exceeding 2.5 μA.

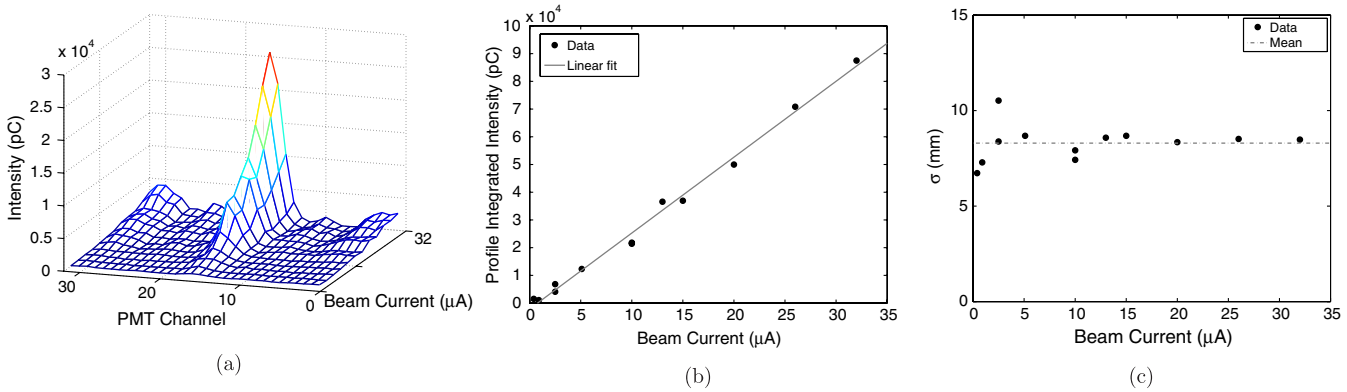

FIG. 6. Beam profiles versus beam current during a systematic scan (a). For each profile, the integrated profile intensity versus the beam current is shown in (b) together with a linear fit ($y = 2737.6$ [pC/μA] $\cdot I_{\text{beam}} - 2107.7$ [pC]). The measured beam width σ versus beam current is shown in (c). The mean width for these data is 8.3 mm.

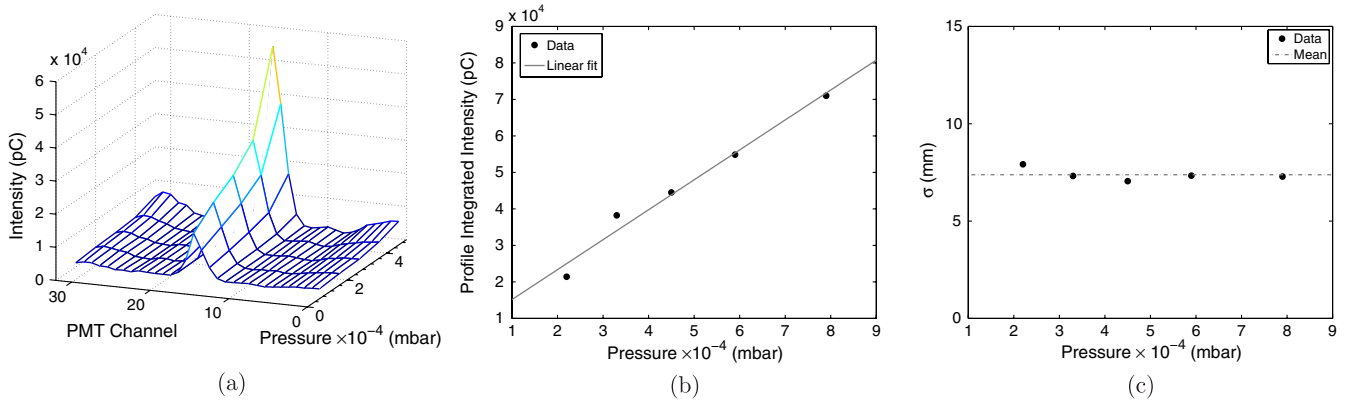

FIG. 7. Beam profiles versus N_2 pressure during a systematic scan (a). For each profile, the integrated profile intensity versus pressure is shown in (b) together with a linear fit ($y = 8.2 \times 10^7$ [pC/mbar] $\cdot P_{\text{gas}} + 6963.1$ [pC]). The measured beam width σ during the pressure scan is shown in (c). The mean size for these data is 7.4 mm

It should be noted that the beam dump was not shielded. Hence, the higher the deuteron beam current, the greater the radiation background, B_R, resulting in an increased background signal at the detectors, B_S, during the measurements. This will be discussed in the next section.

B. Gas pressure scan

The beam current was fixed at 10 μA during the pressure scan. The total integration time was 100 ms and the voltage was again set for maximum gain, while the pressure was raised from 2 to 8×10^{-4} mbar. Although this monitor can be used at lower pressure settings (depending on the beam current and integration time), we are interested in high pressure settings in view of our objective of simulating high beam current scenarios using low beam currents.

Figure 7 shows beam profiles [Fig. 7(a)], integrated profile intensities [Fig. 7(c)], and transverse beam sizes σ(mm) [Fig. 7(c)] versus N_2 pressure. A linear relation between the profile intensity and the pressure was found [see Fig. 7(b)]. Again, a linear fit was performed to the data to highlight the tendency and a slope of 8.2×10^7 pC/ mbar was obtained. In addition, the beam width σ(mm) tends to remain constant when increasing the N_2 pressure [see Fig. 7(c)]. The mean for these data is 7.38 mm, with a standard deviation of 0.32 mm (7.4 ± 0.3 mm).

C. Xenon as residual gas

The beam current scan was repeated using xenon rather than nitrogen as the dominant gas. For this, the xenon pressure inside the beam chamber was held at 8.6×10^{-4} mbar and the beam current range was smaller than for nitrogen, i.e., between 15 and 35 μA. A comparison of the integrated profile intensities and B_S between the N_2 and the Xe experiments is shown in Fig. 8. As the vacuum pressures were different in the experiments, only qualitative comparisons can be made.

The integrated profile intensities [Fig. 8(a)] and B_S [Fig. 8(b)] increase linearly with beam current for both gases. The profile intensities recorded using N_2 [see Fig. 8(a)] are 2.5 times higher than those recorded using Xe, even when the N_2 pressure was 3.6 times lower (2.3×10^{-4} mbar for N_2 versus 8.2×10^{-4} mbar for Xe). Hence, a higher photon yield is found for nitrogen when compared with xenon, at least in the spectral range of maximum detector efficiency (maximum quantum efficiency occurs at 400 nm and drops above 460 nm, falling to zero at 660 nm). This is consistent with earlier work comparing N_2 and Xe, using different beams [5,12].

VII. BACKGROUND SIGNAL DURING MEASUREMENT

Figure 8(a) shows that integrated profile intensities are 150% higher with N_2 than with Xe, although the B_S levels between N_2 and Xe are similar (a 30% higher for N_2). The errors for B_S levels are typically $\pm$10%–15%. Hence, $\partial B_S/\partial I$, the variation of B_S versus beam current, is close to constant for both gases.

If the B_S is due to wall reflections, it should be proportional to the emissivity [Eq. (1)]. In that case, $\partial B_S/\partial I$ should be different for N_2 or Xe because of different emissivities. On the other hand, radiation increases the B_S and the noise in detectors [13], and this seems to be the case here. The major contributor to the B_S is therefore probably the radiation background, rather than reflected or scattered photons. The radiation dose rate is constant for a fixed beam current, independent from the gas used (in the present pressure range). This mechanism can explain the similar B_S levels at different photon yields. Figure 8(c) shows the gamma and neutron radiation doses versus the deuteron beam current, recorded during profile measurements. Both the radiation dose rate and the B_S increase linearly with the beam current.

Reflections off the beam tube walls and their effect on B_S are considered to be less than the contribution due to

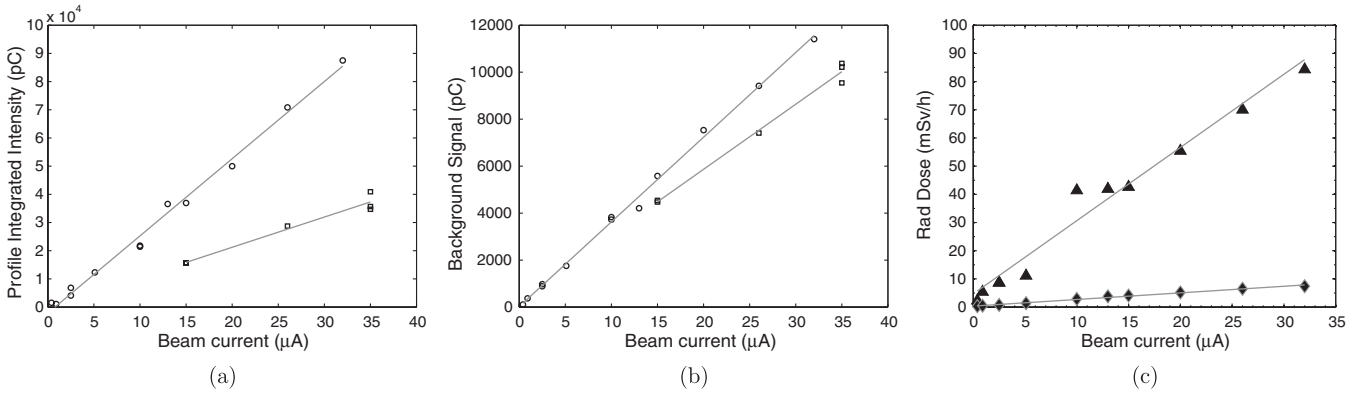

FIG. 8. Integrated profile intensities (a) and B_S (b) using nitrogen (circles) and xenon (squares) plotted versus beam current. Gamma (triangles) and neutron (diamonds) radiation doses registered during the current scan are shown in (c). Linear fits to the data are also shown.

radiation but not completely negligible. This might explain the slightly lower values of B_S for xenon. A beam pipe with a blackened inside surface will reduce the contribution of reflected photons, also preventing profile deformations.

Beam profilers are usually located outside of the shielded target area. For this work, the beam profilers and the beam dump were located in the same vault (Fig. 1) and were subjected to a significant radiation background during the measurements [see Fig. 8(c)]. Although FPMs were capable of measuring with this gamma background, shielding the FPMs will improve the measurements and the operational life of the detector in intense radiation environments.

VIII. FUTURE WORK

A spectral filter could be placed in front of the lens to select a specific line transition, at the cost of reducing photon statistics. The filtering option adds high flexibility to FPMs by providing a way to deal with possible profile distortions. In the case of beams with a high space charge, transitions with short lifetimes can be selected to reduce the particle drift effect during the decay time. A filter wheel will be developed and installed in front of the detector lens to improve the future performance of the profilers.

As this is a work in progress, some improvements still need to be made before installation at LIPAc. New tests with blackened walls to avoid reflections off the beam pipe walls will be performed. The contribution of the radiation background (gammas-neutrons) versus reflected photons will be thoroughly analyzed in the near future. Future work includes the design of a dedicated calibration pattern, a mirror in the optical path for profilers close to target areas (to allow better shielding), or the integration of electronics into the EPICS [14] based local control system.

IX. CONCLUSIONS

Two prototypes for noninterceptive profile monitors based on gas fluorescence, have been designed for the LIPAc accelerator. First in-beam tests have been carried out successfully with a deuteron beam at the CNA cyclotron. Measurements were performed under varying experimental conditions and the observed tendencies have been highlighted. Systematic scans of the beam current and gas pressure show the consistency and reliability of this beam profile technique. The gamma and neutron background contribution to the measurement B_S level of the detectors is subject to further study. As this is a work in progress, some improvements must still be made in the near future, such as implementing a blackened vacuum chamber, a filter wheel, and a dedicated calibration pattern.

ACKNOWLEDGMENTS

This work has been partially funded by the Spanish Ministerio de Ciencia e Innovación Project No. ENE2009-11230/FTN, Diagnostics and Techniques for future particles Accelerators NETwork DITANET project, PITN-GA-2008-215080 and the project FPA2009-08848 from Spanish Ministerio de Ciencia e Innovación, and the excellence project P07-FQM-02894 supported by Junta de Andalucía.

[1] P. Garin, in *Proceedings of the 11th European Particle Accelerator Conference, Genoa, 2008*, edited by C. Biscari and C. Petit-Jean-Genaz (EPS-AG, Genoa, Italy, 2008), TUZG01 [http://accelconf.web.cern.ch/AccelConf/e08/papers/tuzg01.pdf].

[2] M. Plum, E. Bravin, J. Bosser, and R. Maccaferri, Nucl. Instrum. Methods Phys. Res., Sect. A **492**, 74 (2002).

[3] A. Variola, R. Jung, and G. Ferioli, Phys. Rev. ST Accel. Beams **10**, 122801 (2007).

[4] T. Tsang, S. Bellavia, R. Connolly, D. Gassner, Y. Makdisi, T. Russo, P. Thieberger, D. Trbojevic, and A. Zelenski, Rev. Sci. Instrum. **79**, 105103 (2008).

[5] F. Becker, C. Andre, P. Forck, R. Haseitl, A. Hug, B. Walasek-Hoehme, F. Bieniosek, and D. H. H. Hoffmann, in the 9th European Workshop on Beam Diagnostics and Instrumentation for Particle Accelerators, edited by Jan Chrin, Michaela Marx, Volker R. W. Schaa, and Volker Schlott (2009), TUPB02 [http://dipac09.web.psi.ch/Proceedings/papers/tupb02.pdf].

[6] Centro de Investigaciones Energéticas, Medioambientales y Tecnólogicas (CIEMAT) [http://www.ciemat.es].

[7] Centro Nacional de Aceleradores (CNA) [http://intra.sav.us.es:8080/cna/index.php/en].

[8] F. Becker, C. Andre, P. Forck, and D. H. H. Hoffmann, in the 8th European Workshop on Beam Diagnostics and Instrumentation for Particle Accelerators, edited by Ivan Andrian and Volker R. W. Schaa (2007), MOO3A02 [http://accelconf.web.cern.ch/AccelConf/d07/papers/moo3a02.pdf].

[9] Thermo Scientific Inc. [http://www.thermoscientific.com/wps/portal/ts/HOME].

[10] Proxitronic Detector Systems GmbH [http://www.proxitronic.com/].

[11] Hamamatsu Photonics [http://www.hamamatsu.com/].

[12] C. Bohme, T. Weis, V. Kamerdzhiev, J. Dietrich, and J. L. Conradie, in the 9th European Workshop on Beam Diagnostics and Instrumentation for Particle Accelerators, edited by Jan Chrin, Michaela Marx, Volker R. W. Schaa, and Volker Schlott (2009), TUPB10 [http://accelconf.web.cern.ch/accelconf/d09/papers/tupb10.pdf].

[13] S. Hutchins, M. Facchini, and E. Tsoulou, in the 7th European Workshop on Beam Diagnostics and Instrumentation for Particle Accelerators, edited by Volker R. W. Schaa (2005), CTWA02 [http://accelconf.web.cern.ch/AccelConf/d05/PAPERS/CTWA02.PDF].

[14] Experimental Physics and Industrial Control System (EPICS) [http://www.aps.anl.gov/epics/].